Korean J. Chem. Eng., 38(5), 885-898 (2021)
DOI: 10.1007/s11814-020-0739-3

pISSN: 0256-1115
eISSN: 1975-7220

INVITED REVIEW PAPER

Recent applications of the liquid phase plasma process

Sang-Chai Kim*, Young-Kwon Park, and Sang-Chul Jung***,†**

*Department of Environmental Education, Mokpo National University, Muan-gun 58554, Korea
**School of Environmental Engineering, University of Seoul, Seoul 02504, Korea
***Department of Environmental Engineering, Sunchon National University, Sunchon 57922, Korea
(*Received 15 October 2020 • Revised 27 December 2020 • Accepted 29 December 2020*)

Abstract–In this paper, the principle and application of plasma are briefly described, and in particular, the principle and practical application for plasma generated in liquid are introduced. Also, the research results of water treatment, synthesis of metal nanoparticle, synthesis of visible light-responsive photocatalyst, synthesis of energy material, and hydrogen gas production, which were tested using liquid phase plasma, are introduced. Various water pollutants were treated and hydrogen gas was produced using the strong chemical oxidizing species and ultraviolet rays in the plasma field generated in the reactant aqueous solution during the liquid phase plasma (LPP) process. The effects of plasma discharge conditions, dissolved oxygen concentration, pH value, photocatalytic behavior, as well as the properties of organic solutions on the LPP reaction were investigated experimentally and reported. Based on these previous studies, metal nanoparticles were synthesized using hydrogen atom radicals as well as the numerous electrons in the plasma field generated during the LPP process. Additionally, these studies indicate that visible light-responsive photocatalysts can be obtained when metal nanoparticles are precipitated in TiO_2. They also provide evidence that metal nanoparticles can be precipitated in various carbon materials for application as electrodes in secondary batteries and supercapacitors. Therefore, the LPP process has been successfully applied in various fields given that it can be easily and conveniently used, and presently it is being applied in several new fields and many possibilities for its future application are expected.

Keywords: Liquid Phase Plasma, Water Treatment, Metal Nanoparticles, Hydrogen Production, Energy Material

INTRODUCTION

The plasma state refers to a state of matter in which a gas is heated to an ultra-high temperature such that it ionizes, releasing electrons and forming positively charged ions. The physical properties of matter in such a state are clearly distinct from those of matter in other states; thus, the plasma state is considered as the fourth state of matter. Specifically, the plasma state constitutes 99% of the materials that make up the universe, and generally it is divided into the low- and high-temperature plasma states depending on temperature.

The low-temperature plasma state is obtained via glow discharge and arc discharge, with application in various industrial fields, including plasma display panel (PDP) production, semiconductor manufacturing, air purifier manufacturing and fluorescent lamp production. An example of matter in the high-temperature plasma state is the sun, which is a celestial body that is bound by gravity. High-temperature plasma can also be used commercially, e.g., plasma generated in a fusion reactor, and for various reasons it is expected that fusion energy will have application as a next-generation energy source.

Depending on the state of the material within which it is generated, plasma can be divided into three phase regions--gaseous, liquid and solid phase regions--and the relationship between these three plasma phases is shown in Fig. 1. Reportedly, gas phase plasma, which has application in various industrial fields, can be categorized based on different conditions, including low temperature, high temperature, low pressure, atmospheric pressure and high pressure. However, in a metal that is in the solid phase, delocalized electrons move freely between the positively charged metal ions at the lattice points. Such a state consisting of delocalized electrons and positively charged metal ions can be regarded as plasma and can be called solid phase plasma. The collective oscillations of the delocalized electrons, referred to as plasma oscillations, propagate as charge density waves. This vibration is quantized as a particle and is called a plasmon, and the related academic field, which is

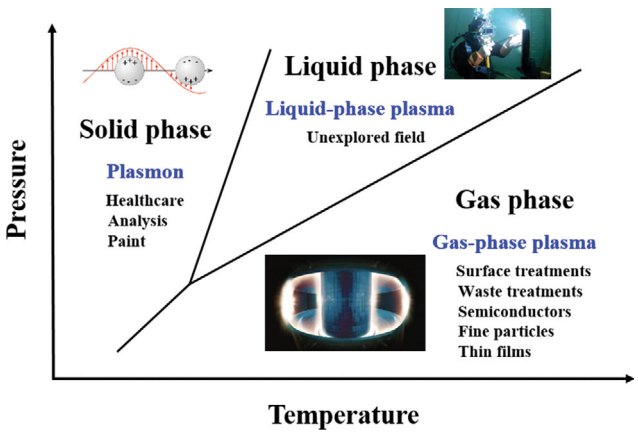

Fig. 1. Plasma applications in various phases.

†To whom correspondence should be addressed.
E-mail: jsc@sunchon.ac.kr

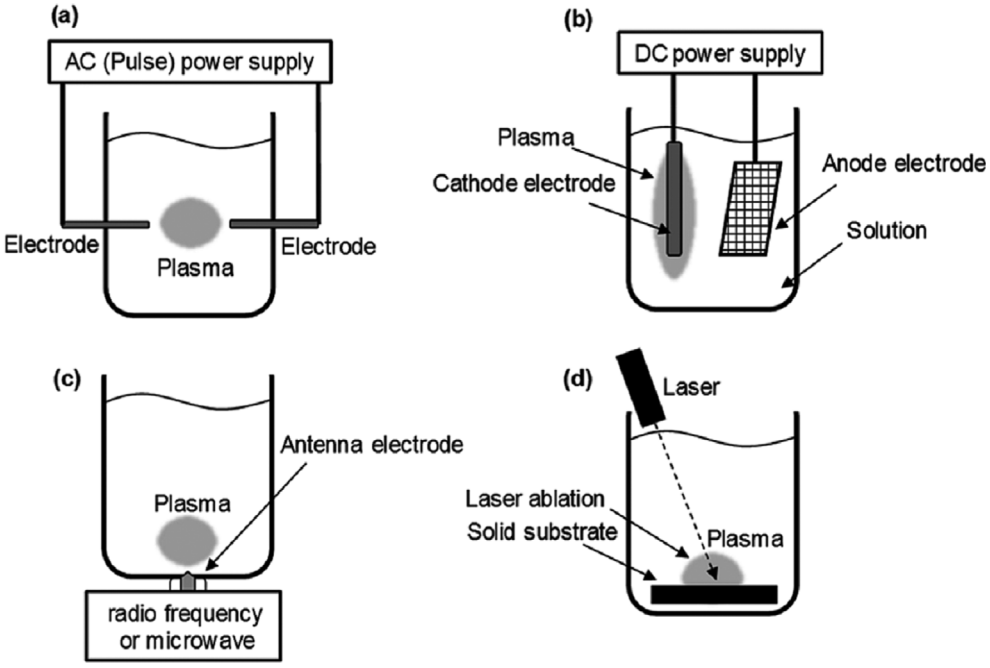

Fig. 2. Images of plasma generation method in a liquid: (a) Direct discharge between two electrodes using an AC (plus) power supply; (b) contact discharge between an electrode and the surface of the surrounding electrolyte using a DC power supply; (c) plasma generation with radio frequency or microwave irradiation; (d) plasma generation using the laser ablation method. Reproduced from ref. [17]. Copyright 2017 by RSC.

beginning to grow, is called plasmonics, as opposed to electronics and photonics, which are related electrons and light, respectively.

However, plasma generated in the liquid phase has received little or no attention until recently. Since ancient times, the phenomenon of electric discharge in liquids has been applied in technologies, including electric discharge machining, hyperbaric welding, electric carburizing and liquid insulation. However, research on the basic physical and chemical properties of plasma in the liquid phase is limited, and recently it has been referred to as arc discharges in water, glidarc discharges in water, or water plasma, and it is being studied gradually. In the 2000s, Nagoya University research, called solution plasma, began to attract attention [1-5].

There are two ways to generate plasma in a liquid phase; the first is a type of corona discharge, a streamer discharge that generates plasma from linearly arranged electrodes using dielectric breakdown in the liquid. Due to dielectric breakdown, the temperature around the heated electrodes rises, generating microscopic bubbles and a plasma field is generated from these bubbles [6]. To perform this plasma discharge, electric power of 200-300 kV and a current of 120 A or more are required in the liquid, and there are problems of maintaining stability and saving energy. Using a pulse voltage in the order of μs, a liquid phase plasma field is generated in a liquid that vaporizes at the liquid-air interface [7,8]. When corona discharge occurs in a liquid phase, the generated plasma field emits various chemically active species, numerous electrons, localized heat, shock waves and ultraviolet rays [9]. The second method is to introduce a gas into the liquid by heating to create a plasma field in the generated bubbles. Insulation breakdown of liquid is not always accompanied by the application of power, and in some cases plasma fields can be generated even with power of 20 kW or less by corona discharge, glow discharge and arc discharge [10-14].

Fig. 2 presents a schematic diagram of the four methods of forming a plasma field in a liquid. The schematic diagram of the plasma field generation in the liquid phase shown in Fig. 2(a) is a form of direct discharge in the form of electric spark discharge and arc discharge on two electrodes. Two electrodes of the same shape and size are installed in a liquid at short intervals and plasma is generated in most liquids containing various solution media or conductive electrolytes by direct discharge. In addition, when current is applied to electrodes installed in a liquid phase, a liquid plasma field is generated and the solution used at this time needs conductivity [15-17].

Ingram and Hickling presented a contact glow discharge electrolysis method as shown in Fig. 2(b). A high-temperature plasma field is formed in the electrolyte around the electrode due to the high electric field, which causes glow discharge light to be emitted. Two electrodes with different electrode surface areas are installed in the electrolyte solution at a distance of 10 to 100 mm and at this time, the electrode with a small surface area is covered with a thin water vapor film that generates electric discharge. This method uses a direct current power source and when current is passed through the electrolyte from the electrode, bubbles are created by Joule heating and a plasma field is created on the cathode side. In this method, it is important to control the conductivity because the condition in which plasma is generated varies depending on the conductivity of the solution. In general, as shown in Fig. 2(b), a mesh metal plate with a large surface area is used for the cathode

and a metal wire is used for the anode and a DC power supply is mainly used, but pulsed DC can also be used.

Fig. 2(c) shows a schematic diagram of a method of forming a plasma field in a liquid by irradiating radio frequency or microwave to the antenna electrode. This method can form a plasma field in a liquid with low power and does not require an electrolytic solution with other methods. Meanwhile, in this method, the dielectric constant and dielectric loss of the solution are important variables for plasma field generation. The radio frequency or microwave used here can be maintained over a wide range of solution conductivity, and low pressure is required because energy is absorbed by water due to dielectric constant and dielectric loss. The biggest advantage of this method is that a plasma field is formed even in pure water, so it can be applied in various fields.

Finally, a schematic diagram of a method of generating plasma balls on a solid surface by irradiating a laser to a solid substrate in a solution is shown in Fig. 2(d). Currently, this method is being used for research such as nanoparticle production [18] and deep sea mass spectrometry [19]. Methods of generating plasma in these liquids have been subdivided by Saito and Akiyama based on engineering diagrams according to operating conditions, reaction conditions and equipment [20]. Meanwhile, new technologies are being reported, such as UV-curing, developed to carry out the process in a sustainable manner [21-26].

In this study, plasma was generated with a similar device and system shown in Fig. 2(a). And in this paper, the concept and system of the liquid phase plasma (LPP) method are explained, and the results of water treatment, synthesis of metal nanoparticle, synthesis of visible light-responsive photocatalyst, synthesis of energy material and hydrogen gas production by applying this method are described.

THEORY OF LPP

Until recently, LPP processes were only used as processing techniques, e.g., in the welding and cutting of metals. This type of LPP, a thermally parallel plasma type that uses temperatures ≥6,000 K as energy source for material processing, is classified as an arc discharge. In recent years, an AC pulse power source has been developed and it has become possible to generate LPP via the inclusion of non-parallel plasma [27]. Additionally, this AC pulse power uses the reaction fields resulting from the formation of the LPP owing to the action of laser, microwaves, and high frequencies [28-30].

Fig. 3 shows a conceptual diagram of LPP generation. Specifically, bubbles are generated around the heated tungsten electrode by the AC power supplied by the pulses, and plasma is formed within these generated bubbles and not directly in the liquid. Five effects, including electromagnetic field generation, UV radiation, overpressure shock wave generation, the generation of various free radicals and ozone generation with O_2 bubbling, occur simultaneously in the LPP field thus formed [31-33]. These phenomena occurring in the plasma field can be applied in various synthesis and decomposition processes [34-36]. Particularly, metal ions in the LPP reaction precursor aqueous solution can be reduced by the numerous electrons generated in the plasma field and precipitated into the metal particles. Further, metal nanoparticles can be precipitated in various substrates (e.g., various carbon materials and TiO_2) through this reduction reaction. Additionally, organic pollutants in water can be treated using strong oxidizing agents, such as the hydroxyl radicals (OH·) generated in the LPP field, and water or organic solvents can be decomposed by the strong plasma field; thus, hydrogen can be produced easily.

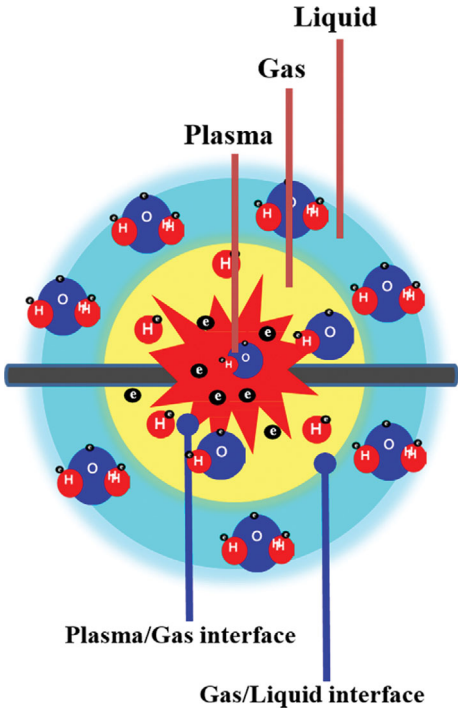

Fig. 3. The concept of liquid phase plasma process.

DEVICE

The different devices used in the LPP process differ slightly depending on the field of application; however, the fundamental elements of the critical equipment are the same [37-39]. Here, representatively, the experimental equipment used for water treatment, which is shown on the left side of Fig. 4, is described. Plasma is generated in the liquid using a power supply that pulses direct current. To clean the electrodes, ensure stable operation and generate a symmetrical plasma, the DC power is supplied as a bipolar pulse. In these LPP studies, the power supply is operated at an applied voltage in the range 200-250 V, a pulse width in the range 1-5 μs, and a frequency in the range 10-30 kHz. Pulsed discharge is performed on a tungsten electrode installed in a double annular or cylindrical quartz reactor.

To prevent the rise in the temperature of the LPP reaction aqueous solution due to plasma discharge, a cooling water bath is used. In the water treatment experiment, a dissolved oxygen generator is used to change the dissolved oxygen concentration in the aqueous reactant solution. However, for nanoparticles synthesis and hydrogen production processes, the dissolved oxygen generator is not used, but all the other components of the devices used are basically the same.

The current and voltage applied to the LPP are detected using a

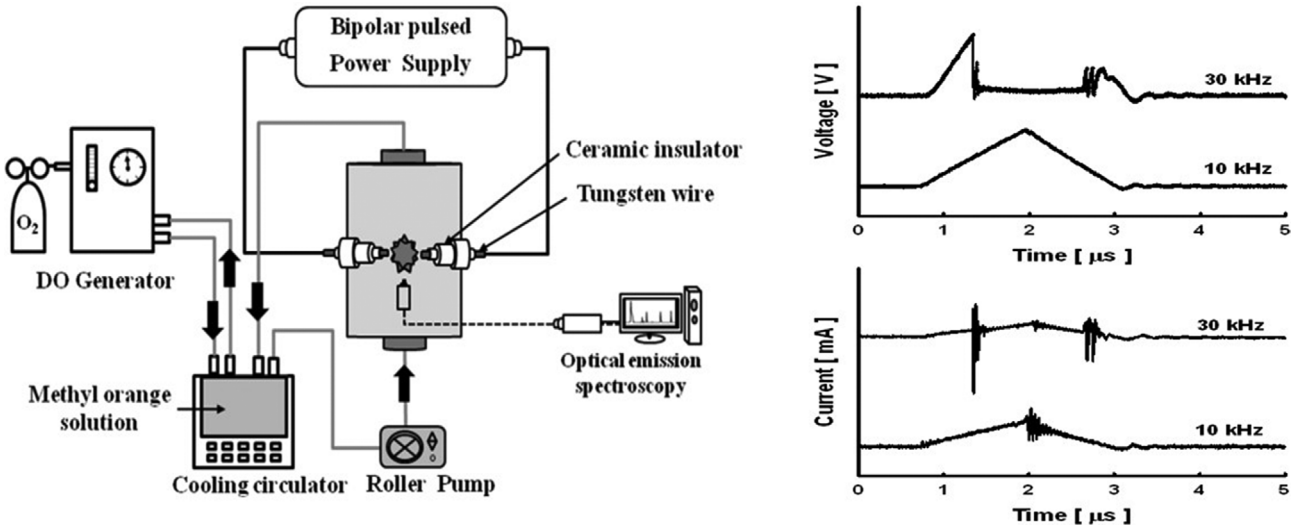

Fig. 4. Liquid phase plasma device and shape of breakdown.

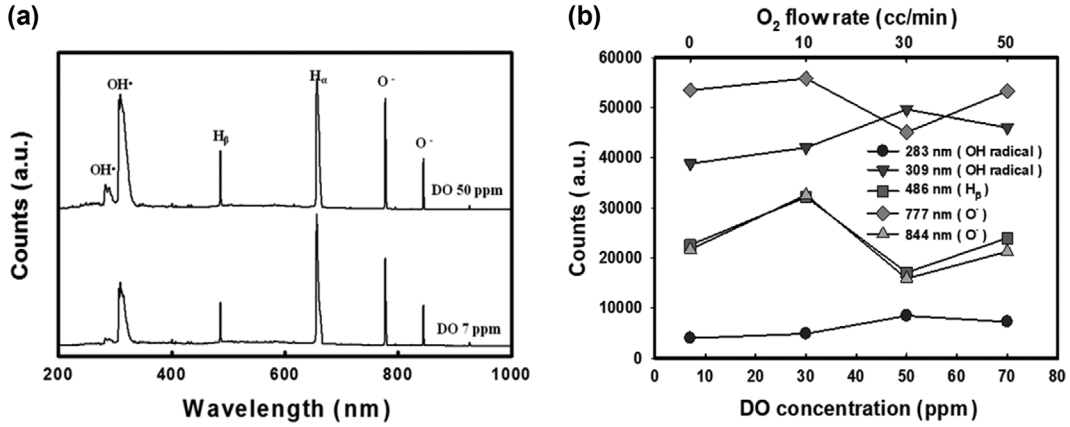

Fig. 5. Optical emission spectrum in the plasma field generated by LPP radiation and changes in the generated radicals. Reproduced from ref. [42]. Copyright 2015 by Taylor & Francis.

probe connected to a digital oscilloscope. The energy and power per pulse collected by the oscilloscope are calculated as the product of the voltage and the current. The obtained current and voltage waveforms are shown on the right side of Fig. 4. These quantities are measured by changing the frequency to 30 and 10 kHz under an applied voltage and pulse width of 250 V and 5 μs, respectively. Fluid breakdown is observed at 30 kHz, and not at 10 kHz. This breakdown resulted from an increase in voltage and current dissipated heat from the dielectric, and plasma was generated owing to the rapid increase in resistance and the rapid drop in voltage.

APPLICATIONS OF THE LPP PROCESS

1. Water Treatment

Various water pollutants were successfully degraded using the LPP process [40-42]. In this section, the results of a methyl orange degradation experiment based on a dissolved oxygen generator coupled the LPP system are presented [43].

In the degradation of organic pollutants using the LPP system, the strong oxidizing radicals generated in the plasma field play a very important role. Therefore, the concentrations of the generated chemically reactive species were measured using an optical emission spectrometer, and the optical emission spectra corresponding to distilled water (DI) water (7 ppm) and water with a high dissolved oxygen concentration (50 ppm) are shown on the left side of Fig. 5. These spectra show the presence of the hydroxyl radical (OH·), atomic hydrogen (H_α and H_β) and atomic oxygen [44]. Very rapid reactions were induced by these chemically active radicals, that were generated in the powerful plasma field of the LPP. Thus, metal ions were reduced by the generated atomic hydrogen radicals, and several electrons resulted in the precipitation of metal nanoparticles [45], while oxygen radicals and hydroxyl radicals, with strong oxidizing power, oxidized organic pollutants to inorganic species. At higher dissolved oxygen concentration, there was an increase in the number of photons in the activated species, especially in the hydroxyl radicals. Based on the results obtained, it is evident that increasing the concentration of hydroxyl radicals by increasing the dissolved oxygen concentration is an effective strat-

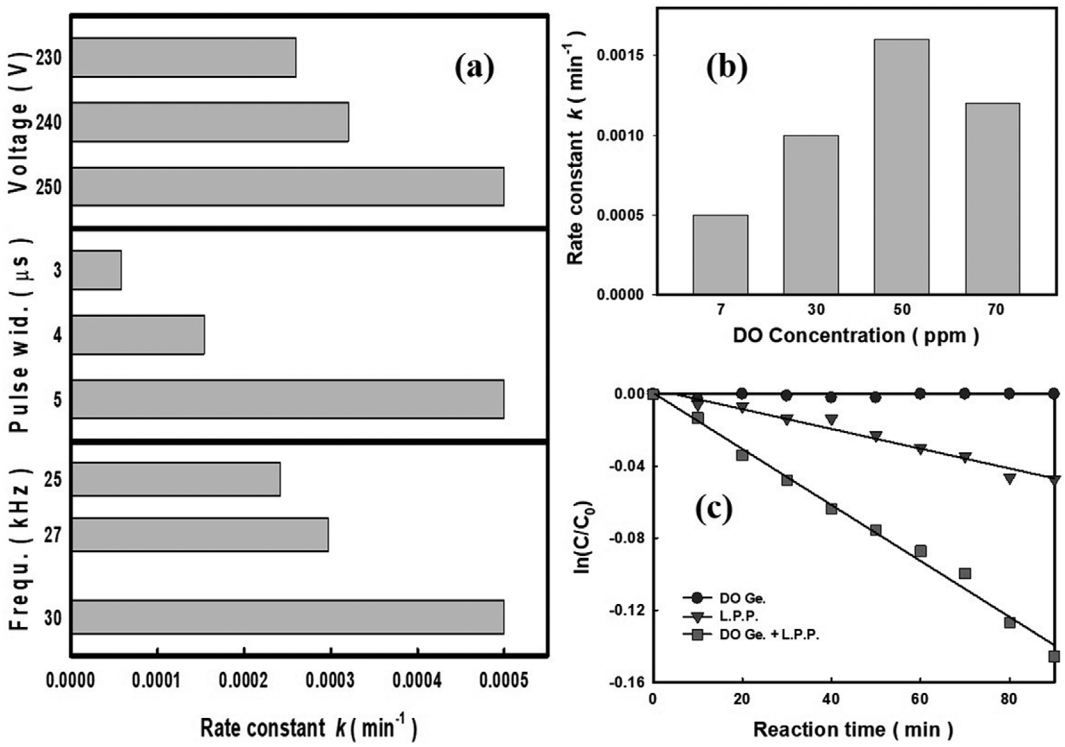

Fig. 6. (a) Methyl orange decomposition rate obtained with different levels of impressed voltage, pulse width and frequency. (b) Degradation rate of methyl orange measured at various dissolved oxygen levels. (c) Comparison of the methyl orange decomposition rate obtained under different experimental conditions. Reproduced from ref. [42]. Copyright 2015 by Taylor & Francis.

egy in the degradation of water pollutants.

The photons count change based on the optical emission spectra of O·, OH· and Hβ· radicals with respect to changes in dissolved oxygen concentration is shown in Fig. 5. The number of photons in the OH· radicals increased up to a dissolved oxygen concentration of 50 ppm but decreased when the dissolved oxygen concentration reached 70 ppm. This phenomenon could be attributed to the scavenging effect of the recombination of the OH· radicals. Additionally, the number of photons in Hβ· and O· is inversely correlated with the number of photons in OH·.

Fig. 6(a) shows the variation in the rate of methyl orange degradation when the plasma discharge conditions (pulse width, frequency and voltage) were changed. As the applied voltage increased, the rate of methyl orange degradation tended to increase. This observation could be attributed to the strong plasma field that was established by the high applied voltage. Additionally, as the pulse width increased, the rate of methyl orange degradation also tended to increase. This is because an increase in the pulse width resulted in an increase in the plasma production time. Further, as the frequency increased, the rate of methyl orange degradation also tended to increase owing to the generation of a good number of OH· radicals as a result of the large discharge [42].

Fig. 6(b) shows the effect of dissolved oxygen concentration on the rate of methyl orange degradation using the LPP process. From this figure, it is evident that the degradation rate increased (0.0016 min^{-1}) as the dissolved oxygen concentration increased to 50 ppm. However, at a dissolved oxygen concentration of 70 ppm, a decrease in the decomposition rate was observed (0.0012 min^{-1}). This finding is correlated with the photon count associated with the OH· radicals. Thus, it is evident that OH· radicals play a very important role in the degradation of water pollutants during the LPP process.

Fig. 6(c) shows the variation of the rate of methyl orange degradation under various degradation experimental conditions. "DO Ge." represents an experiment that was performed using only the dissolved oxygen generator (50 ppm). Under these experimental conditions, almost no degradation was observed. However, when the LPP process was coupled with the dissolved oxygen generator, there was a three-fold increase in the degradation rate compared with that observed when only the LPP process was used.

2. Synthesis of Nanoparticles

Using the LPP process, a variety of nanosized single-component metal particles, as well as two-component bimetallic nanoparticles, were successfully synthesized. Here, the results obtained following the application of the LPP process in the synthesis of Sn nanoparticles and Fe-Ru bimetallic nanoparticles are presented [46,47].

Fig. 7(a) shows the FETEM images of the Sn nanoparticles that were synthesized via the LPP method using reactant aqueous solutions with different cetyltrimethylammonium bromide (CTAB) concentrations (i.e., 0, 10, 30 and 50 mol%). In the absence of CTAB, the Sn particles obtained had sizes in the range 30-90 nm and were partially agglomerated. However, the addition of CTAB resulted in well dispersed smaller particles. Further, when the molar concentration of CTAB was 50%, the average size of the Sn particles obtained was below 10 nm and the particles showed a very high degree of dispersion [32].

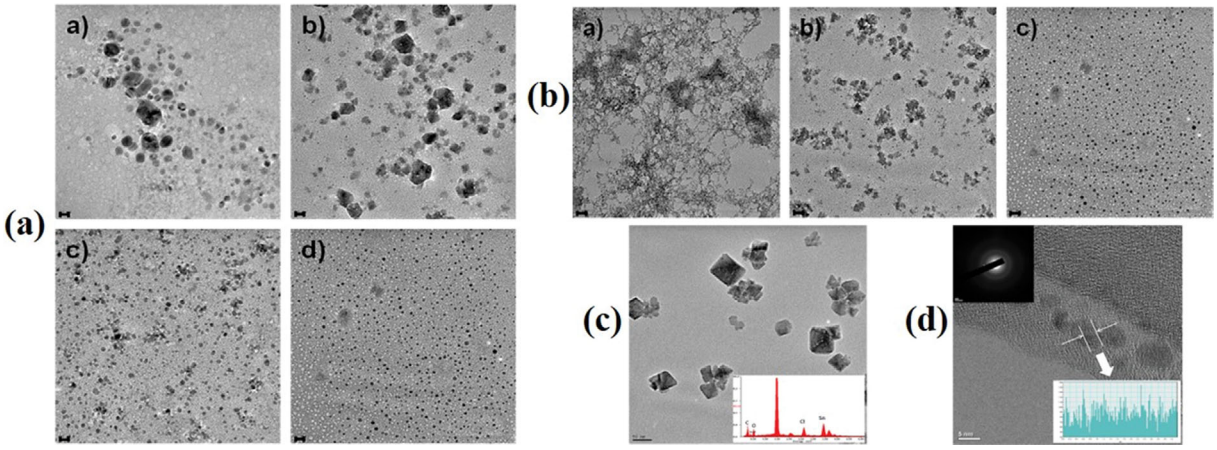

Fig. 7. (a) TEM images of Sn nanoparticles synthesized with different CTAB molar ratio in the solution: a) 0%, b) 10%, c) 30%, d) 50%. (b) TEM images of Sn nanoparticles synthesized with different discharge time: a) 10 min, b) 30 min, c) 50 min. (c) FETEM image and EDS spectrum of tin dioxide in the white slurry synthesized using LPP process, HR-FETEM images and corresponding ED patterns of Sn nanoparticles synthesized using LPP process. Reproduced from ref. [32]. Copyright 2017 by American Scientific Publishers.

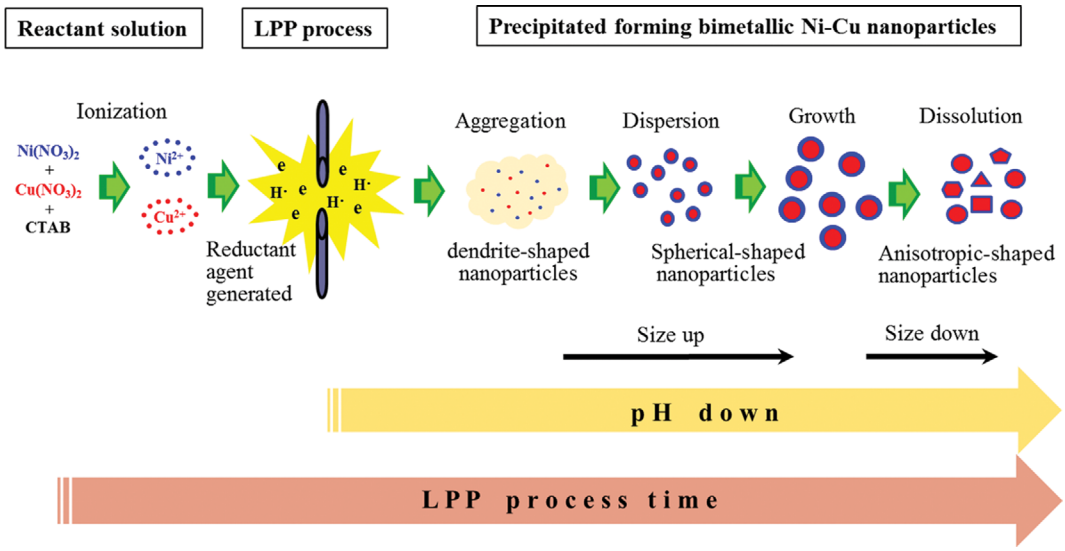

Fig. 8. Formation mechanism of Ni-Cu bimetallic nanoparticles synthesized with plasma in the liquid phase. Reproduced from ref. [31]. Copyright 2016 by The Korean Institute of Chemical Engineers.

The variation of the shapes of the Sn particles obtained using the LPP process with process time based on TEM are shown in Fig. 7(b). At 10 min into the LPP process, the Sn particles formed, which had sizes of approximately 70 nm, were dendrite-shaped like. However, as the LPP process time increased, the particles showed a decrease in size. At an LPP process time of 50 min, spherical Sn nanoparticles with sizes below 10 nm that were well dispersed were observed.

Fig. 7(c) shows the results of the FETEM and EDS analyses of the sediment produced via the LPP process. The analysis of the EDS spectrum of the precipitate indicated that the precipitate particles produced with tin and oxygen in the ratio 12 : 23 were SnO_2. Additionally, these precipitated SnO_2 particles, which were tetragonal in shape, had sizes in the range 10-70 nm.

According to Fig. 7(d), which shows the HR-FETEM images of the synthesized SnO_2 particles, the lattice fringes of the spherical SnO_2 particles were approximately 2 Å. Additionally, the ED pattern of the synthesized SnO_2 particles showed that they were amorphous.

Fig. 8 shows the mechanism by which the Ni-Cu bimetallic particles were synthesized using the LPP process. During the initial stage of the LPP reaction, precursor ions were reduced to generate large dendrite-shaped particles. In the second step, the nucleation reaction proceeded rapidly and the bimetallic particles were dispersed into spherical nanoparticles. Concurrently, there was a gradual decrease in the pH of the reaction solution as the reaction time increased; therefore, the decrease in the size of the particles could be attributed to the drop in the pH value. Further, as the LPP process continued, the size of the particles gradually increased and continued to increase, forming anisotropic-shaped particles [31].

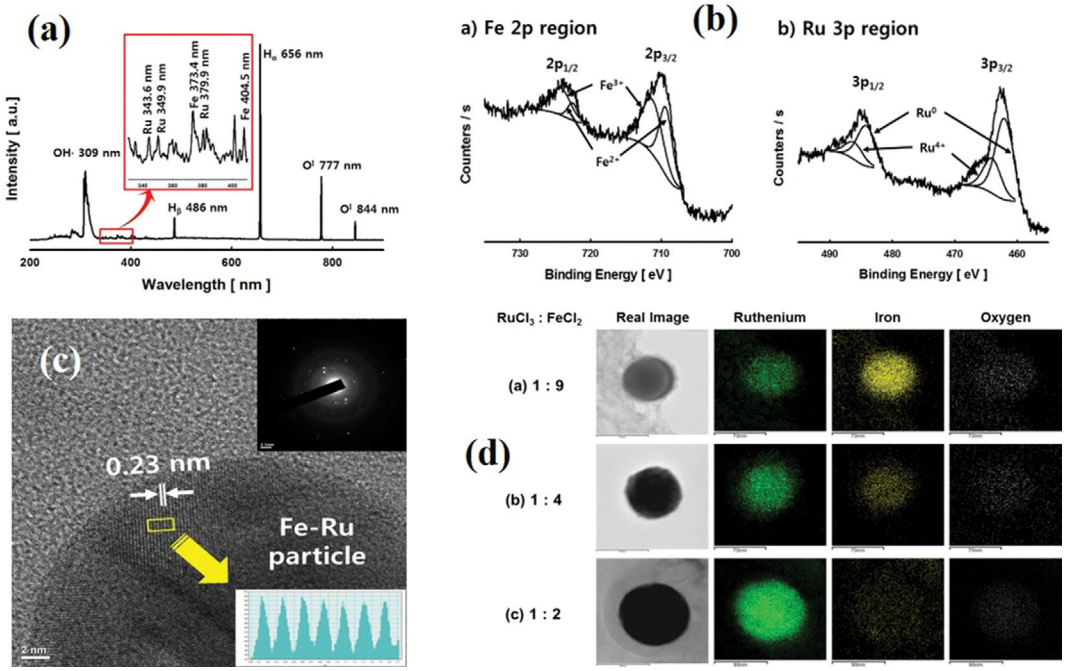

Fig. 9. (a) Spatially and temporally integrated emission spectra for the plasma discharge in iron-ruthenium chloride solution. (b) HR-XPS spectra of bimetallic Fe-Ru oxide nanoparticles. (c) HR-FETEM image and corresponding ED pattern of bimetallic Fe-Ru oxide nanoparticle. (d) HR-FETEM image and individual element mapping result of bimetallic Fe-Ru oxide nanoparticles with different molar ratio of precursor. Reproduced from ref. [46]. Copyright 2016 by Springer.

The emission spectrum obtained when the LPP was applied to the aqueous reaction solution consisting of $FeCl_2$ and $RuCl_3$ is shown in Fig. 9(a). During the measurement, the iron and ruthenium ions observed were reduced by the numerous electrons in the electromagnetic field generated by the LPP and metal particles were precipitated. Additionally, the precipitated metal particles could be oxidized by the large amount of strongly oxidizing species present in the plasma field to generate metal oxide particles [46].

The chemical state of the synthesized Ni-Cu bimetallic particles was analyzed using HR-XPS, and the results obtained are shown in Fig. 9(b). Peaks corresponding to Fe^{2+} and Fe^{3+} were observed, and based on this observation it was considered that the precipitated iron was iron oxide in the forms Fe_2O_3 and Fe_3O_4 [48,49]. Additionally, peaks corresponding to Ru_2 and Ru^{4+} were also observed; thus, is was assumed that the metal Ru and anhydrous ruthenium oxide were precipitated [50,51].

Fig. 9(c), which shows the HR-FETEM image of the Fe-Ru bimetallic nanoparticles, shows that the lattice spacing on the surface of the Fe-Ru bimetallic nanoparticle crystal was approximately 0.23 nm. Additionally, the ED pattern of the bimetallic nanoparticles showed the absence of points and circles, indicating that the synthesized particles were amorphous.

The composition of the Fe-Ru bimetallic nanoparticles obtained following the variation of the initial concentration of the precursor (i.e., to 1 : 9, 1 : 4 and 1 : 2) was analyzed via EDS, and the results obtained are shown in Fig. 9(d). These results confirm that ruthenium was preferentially precipitated over iron owing to its lower ionization tendency and its higher reduction potential. They also confirm that the elemental composition of the Fe-Ru bimetallic nanoparticles can be controlled by the composition of the precursor in the reactant aqueous solution.

3. Visible Light Responsive Photocatalyst

Visible light responsive TiO_2 photocatalysts were successfully synthesized by precipitating various nanometal particles on the surface of TiO_2 using the LPP process. In this section, the results obtained following the preparation of a modified visible light responsive TiO_2 photocatalyst via the doping of TiO_2 with nano-iron particles using the LPP process are presented [52].

Fig. 10(a) shows the HR-FETEM image of the photocatalyst obtained by doping TiO_2 powder with iron nanoparticles (hereafter referred to as IOTP) using the LPP process. The real image of the IOTP, which also shows the electron diffraction pattern of a selected area of the IOTP in which six ring patterns were observed, is shown at the far left of Fig. 10(a). These patterns corresponded to TiO_2 anatase crystals (101, 211, and 220 planes) and iron oxide (Fe_3O_4; 311, 400 and 440 planes) crystals. A high magnification image of the IOTP is shown at the center of Fig. 10(a). From this high magnification image, the 110 and 101 lattice planes of Fe_3O_4 and TiO_2 anatase crystals, respectively, were observed, and their sizes were 0.48 and 0.34 nm, respectively. At the far left of Fig. 10(a), the results obtained based on IOTP element mapping are presented. Based on the detection of iron, titanium and oxygen in the IOTPs, it could be concluded that the TiO_2 surfaces were successfully doped with nano-iron particles [41].

Fig. 10(b) shows the real HR-TEM image of the IOTP as well as the mapping results corresponding to each of the detected elements. The IOTP particles observed in the real image show an average particle size of 25 nm, which is consistent with the P25

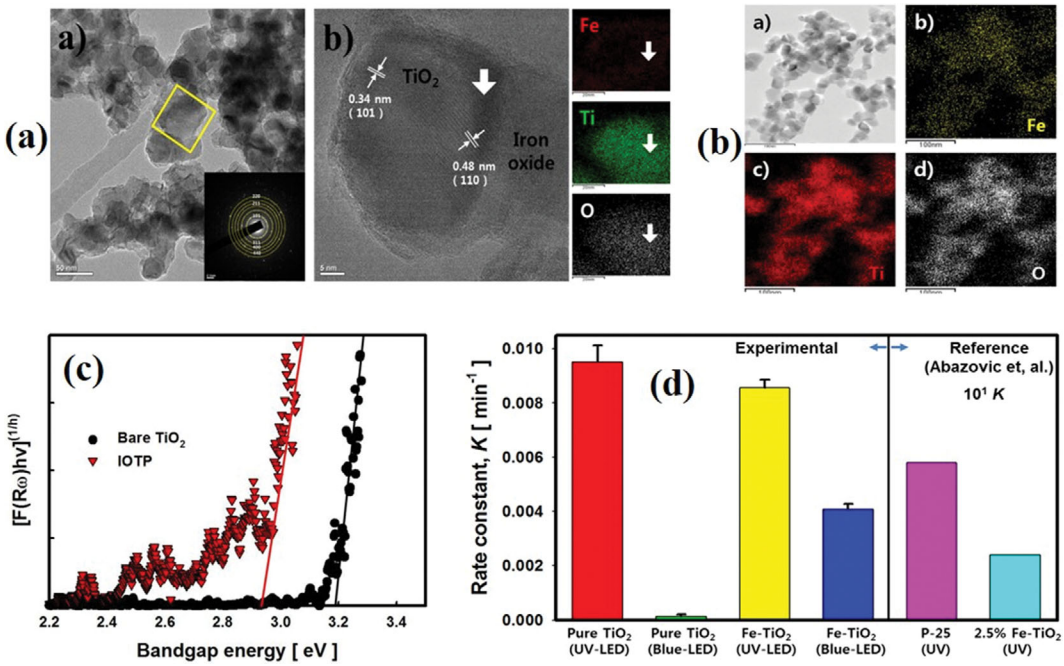

Fig. 10. (a) HR-FETEM image including SAED pattern and high magnification photograph of yellow boxed region showing lattice and mapped element of IOTP powder. (b) HRTEM image of IOTP powder a) and mapped element of IOTP powder prepared by LPP process: iron b), titanium c), and oxygen d). (c) Optical absorbance of bare TiO_2 and IOTP. (d) Rate constants of decomposition reaction using various photocatalysts with different LED lamps. Reproduced from ref. [41]. Copyright 2016 by Elsevier.

size of TiO_2 powder particles used. Further, the distribution images corresponding to the iron, titanium and oxygen elements detected match the shape of the TiO_2 powder. Furthermore, all these elements were distributed very uniformly; thus, it was evident that the synthesis of IOTP was successful.

Fig. 10(c) shows the band gap energies inferred via the measurement of the absorbance of the un-doped TiO_2 powder and IOTP using UV-Vis spectroscopy. The measured band gap energy (Eg) of the undoped TiO_2 was 3.19 eV, which was almost identical to that of the P25 (3.20 eV) used. In contrast, the Eg of IOTP was 2.92 eV, which represents a shift to a lower Eg compared with the un-doped TiO_2. Thus, visible light responsive TiO_2 photocatalysts were successfully prepared using the LPP process.

Fig. 10(d) shows the photocatalytic activity of bare TiO_2 and the prepared IOTP measured using UV and blue LED lamps. The measured degradation reaction rate constants of the un-doped TiO_2 were 9.53×10^{-3} and 1.37×10^{-3} min^{-1} for the UV and blue LED lamps, respectively, and the degradation rate decreased by approximately 99% in blue light than UV light. Additionally, the degradation reaction rate constant corresponding to the prepared IOTP for the blue LED lamp was 4.09×10^{-3} min^{-1}, which represents a 53% decrease compared with 8.58×10^{-3} min^{-1} for the UV LED lamp. From these results, it is evident that preparing visible light-responsive photocatalysts using the LPP process is simple and effective.

4. Energy Materials

Using the LPP process, electrodes for various secondary batteries and supercapacitors were successfully synthesized. Here, the results obtained following the preparation of tin oxide/carbon composites and applying them as electrodes in supercapacitors as well as the results obtained following the preparation of cobalt/graphene sheet composites and applying them as electrodes in lithium secondary batteries are presented [53,54].

Fig. 11(a) shows the FESEM image of the tin oxide/carbon composite (TCC) synthesized via the LPP process, as well as the mapping image corresponding to each detected element. The carbon in the activated carbon powder was clearly mapped and oxygen and tin were uniformly distributed in the same pattern and mapped. In addition, since oxygen and tin had a similar distribution pattern, the precipitated tin was presumed to be tin oxide [45].

Fig. 11(b) shows the low and high magnification TEM images of the TCC prepared using the LPP process. The average size of the SnO_2 nanoparticles precipitated on the activated carbon powder was approximately 5 nm, and the lattice fringes of these SnO_2 nanoparticles were determined to be approximately 3.5 Å. However, the precipitated SnO_2 particles were considered to be amorphous given that their ED patterns showed the absence of circles and spots.

The electrochemical stability of the TCC electrodes synthesized by varying the LPP discharge time was investigated by monitoring charge/discharge cycles, and the results obtained are presented in Fig. 11(c). It was observed that bare activated carbon powder, in which SnO_2 nanoparticles were not precipitated, decreased by approximately 5.5% to 24.43 and 23.07 F/g during the 1st and 20th cycles, respectively. The initial specific capacitance values of the prepared TCCs synthesized by varying the LPP reaction time were all higher than that of the bare activated carbon, and the specific capacitance of the TCC increased as the LPP reaction time increased.

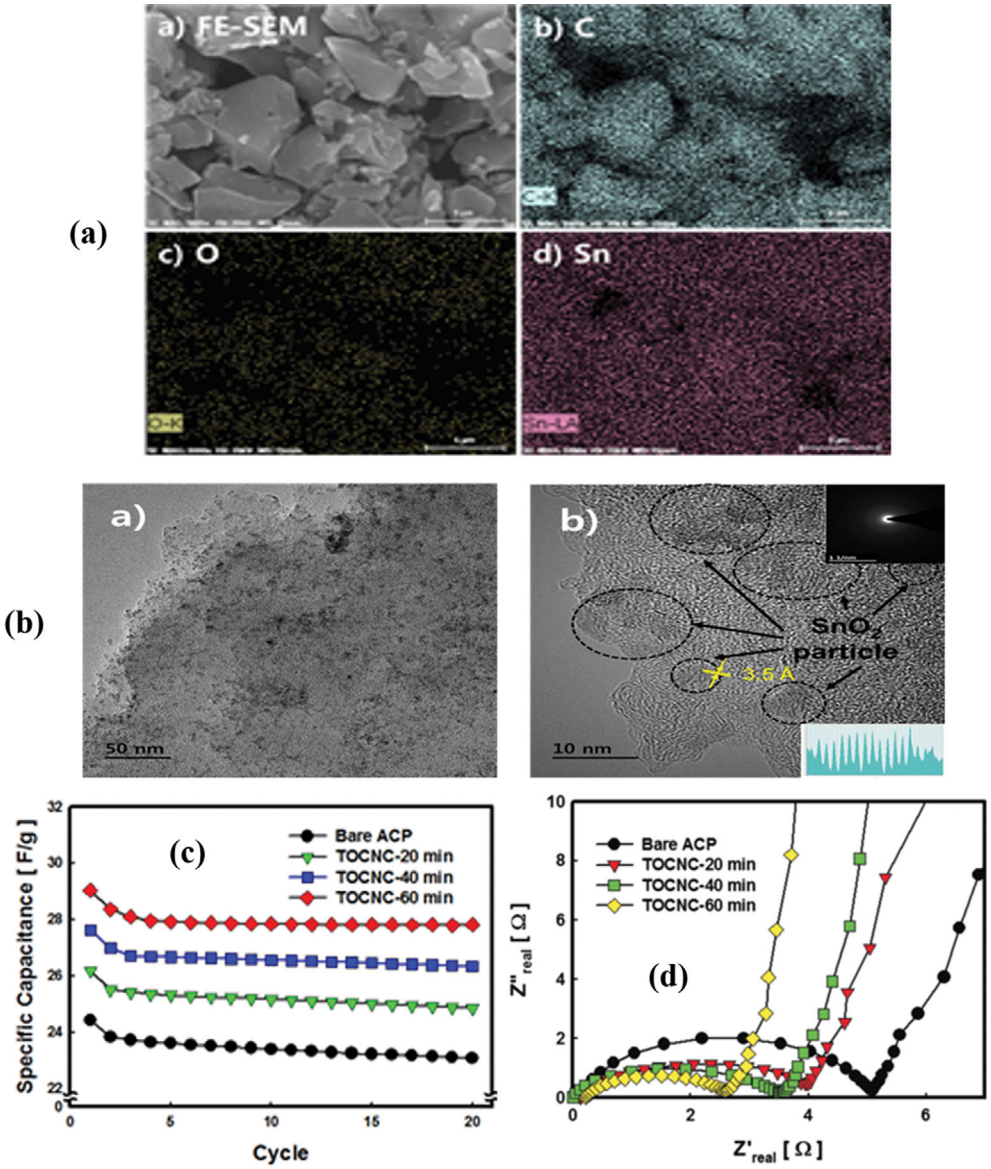

Fig. 11. (a) FESEM images including mapped individual elememt of composite using LPP method: a) FE-SEM image, b) mapped C element, c) mapped O element, d) mapped Sn element. (b) HR-FETEM images of TCC prepared by LPP method: a) low magnification, b) high magnification including ED pattern. (c) Specific capacitance of bare ACP and TCCs as a function of cycling number of charge-discharge. (d) Nyquist plot of bare ACP and TCC electrodes prepared with different LPP duration time. Reproduced from ref. [45]. Copyright 2017 by American Scientific Publishers.

Fig. 11(d) shows a Nyquist plot corresponding to the impedance of a coin cell made from the TCC synthesized under different LPP reaction times and untreated activated carbon powders. The impedance measurement shows that the Rs level of the cathode material was 5.00 Ω while that of the TCC electrode decreased as the LPP discharge time increased. Further, in the lower frequency region, the slope corresponding to the bare activated carbon powder was 3.97, while that corresponding to the TCCs tended to increase as the LPP discharge time increased.

Fig. 12(a) shows the FETEM images corresponding to the graphene sheet (a) and cobalt/graphene composite (CGC) (b) used as electrode materials. The graphene sheet was scrolled into a crumpled shape, and from the CGC images it was observed that cobalt particles with sizes of approximately 5 nm were evenly distributed on the graphene surface [53].

Fig. 12(b) shows the HR-FETEM image of the CGC electrode prepared using the LPP process. The average size of the cobalt nanoparticles that were deposited on the two-dimensional graphene surface was approximately 3-7 nm. However, the precipitated cobalt nanoparticles were presumed to be amorphous, given the absence of circles and spots in their ED pattern.

The electrochemical stability of the CGC electrode prepared using the LPP process was examined by monitoring charge/discharge cycles, and the results obtained are shown in Fig. 12(c). It was observed that the specific capacity of the graphene electrode in which cobalt was not precipitated decreased following the

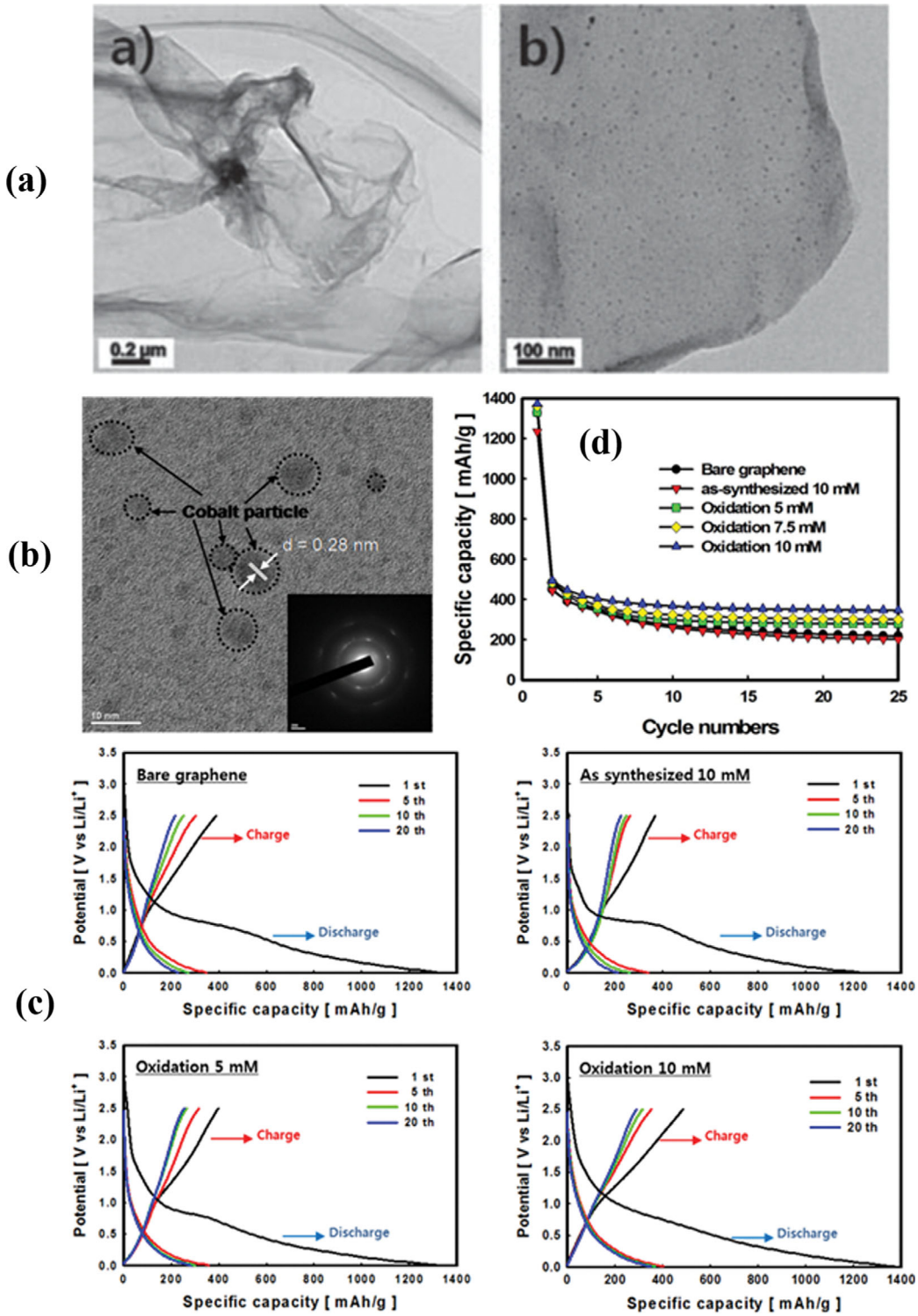

Fig. 12. (a) FE-TEM images of bare graphene sheet and cobalt/graphene composite. (b) HR-FETEM images, including ED patterns of cobalt oxide nanoparticles on the surface of graphene sheet. (c) Charge/discharge curves of bare graphene electrode and cobalt oxide/graphene composite electrode. (d) Cycling performance of bare graphene electrode and cobalt oxide/graphene composite electrodes. Reproduced from ref. [53]. Copyright 2016 by American Scientific Publishers.

repeated charge/discharge cycles. Considering the shape of the discharge curve, the specific capacity of the synthesized CGC electrode was smaller than that of the un-doped graphene electrode. Further, the specific capacity of the heat-treated electrodes, (c) and (d), was 1.33 and 1.38 $mAhg^{-1}$, respectively, and it was determined that the capacity loss due to the repeated charge/discharge cycles

was less than that of graphene in which cobalt was not precipitated.

Fig. 12(d) shows the variation of the lithium storage capacity of the un-doped graphene, CGC, and the heat-treated CGC with the number of cycles. The undoped graphene electrode shows a decrease in specific capacity from 450 to 227 $mAhg^{-1}$, while the CGC electrode shows a decrease from 443 to 212 $mAhg^{-1}$. However, the specific capacity of the heat-treated CGC electrode increased as

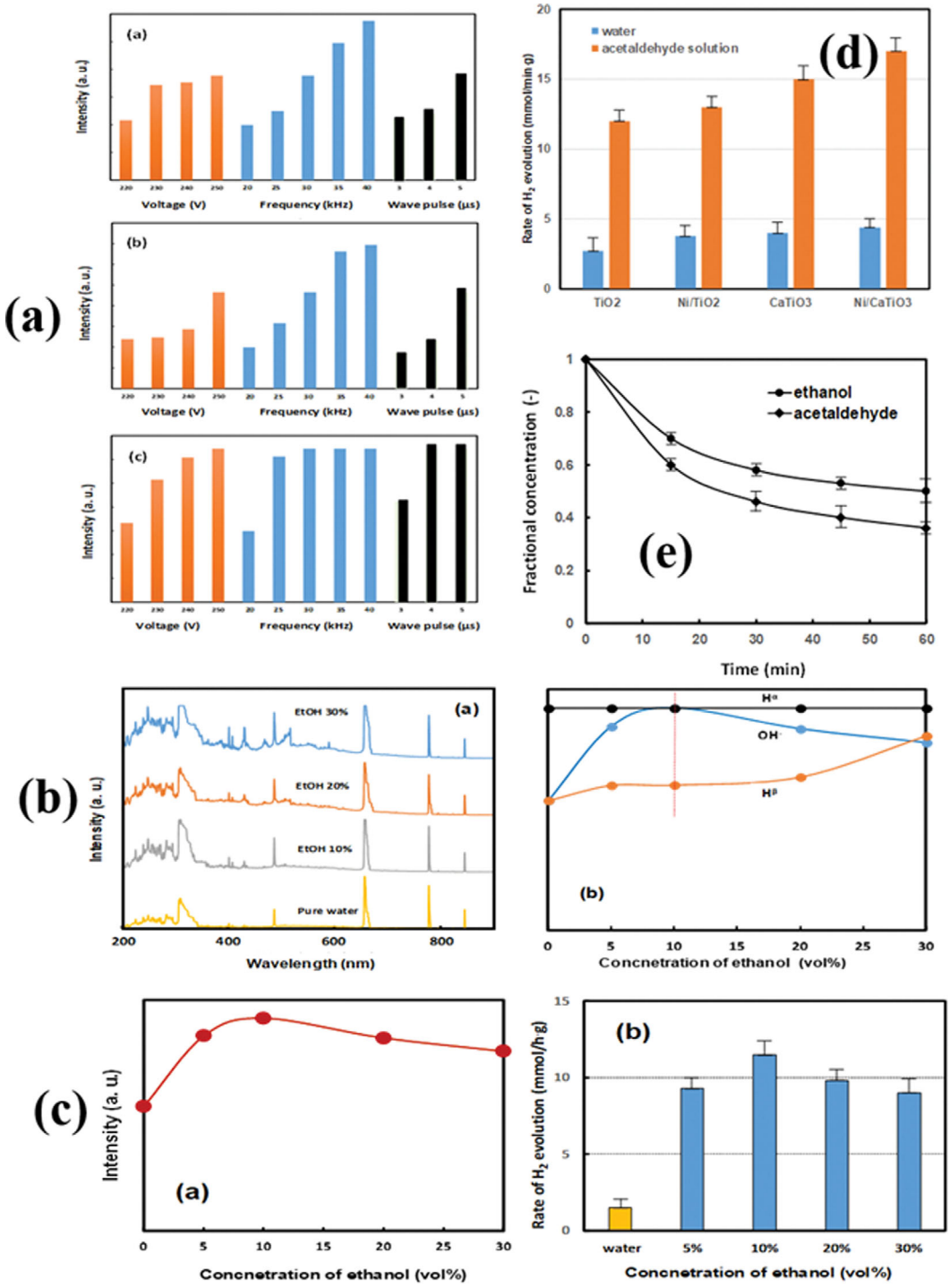

Fig. 13. (a) OES of LPP measured at various wavelength with discharging conditions of LPP generation in distilled water. (b) OES of LPP irradiation in aqueous ethanol solution with various ethanol concentration and variation of main peaks of OES with various ethanol concentrations. (c) Variation of OES intensity of OH· radical peak at 309 nm and rate of hydrogen evolution with various ethanol concentration. (d) Rates of hydrogen evolution in pure water and aqueous acetaldehyde solution on various photocatalysts. (e) Variation of fractional concentration of ethanol and acetaldehyde by photocatalytic decomposition using LPP on Ni/CTO photocatalysts. Reproduced from ref. [57]. Copyright 2018 by Elsevier.

the initial precursor concentration increased and was superior to that of the un-doped graphene electrode.

5. Hydrogen Gas Evolution

Hydrogen was produced from water using the LPP process, and during this process pollutants in different types of wastewater were successfully decomposed [54-56]. Here, the process of producing hydrogen from ethanol and acetaldehyde, while adding a photocatalyst, in the LPP process, is presented [57].

Fig. 13(a) shows the OES detected during LPP emission into DI water, during which various chemically active species, strong UV and visible light were emitted. The spectrum obtained showed peaks corresponding to H_β, H_α, O^I and OH· radicals, and specifically UV light (309 nm) and visible light (609 nm) were largely emitted. With LPP irradiation only, water can be photodecomposed to produce hydrogen gas; however, in the presence of a photocatalyst, hydrogen gas production could be primarily attributed to the action of UV and visible light rather than the action of chemically active species.

The emission spectrum corresponding to the aqueous solutions of the LPP reaction with different ethanol concentrations as well as the change in the wavelength of the main peak is shown in Fig. 13(b). The H_α peak does not change with ethanol concentration; however, it shows a tendency to slightly increase as the ethanol concentration increases. In contrast, the concentration of the OH· radicals was highest in the solution containing 10% ethanol.

Fig. 13(c) shows the variation of the hydrogen production rate with ethanol concentration. When ethanol was added, the rate of hydrogen production increased remarkably, and the generation of hydrogen gas was most effective in the solution containing 10% ethanol. Additionally, OH· radicals show the largest peak in the spectrum corresponding to the 10% ethanol solution (309 nm), and it was estimated that the superior hydrogen generation activity was due to the photolysis reaction induced by the OH· radicals.

Fig. 13(d) shows the rate of hydrogen production in DI water and acetaldehyde aqueous solution. From the figure, it is evident that $CaTiO_3$ resulted in a higher hydrogen generation efficiency than TiO_2. Further, the addition of Ni to $CaTiO_3$ resulted in a hydrogen production rate that was higher than that corresponding to bare $CaTiO_3$, which increased as the amount of acetaldehyde increased. The results corresponding to the decomposition of ethanol and acetaldehyde using the LPP method with the addition of a photocatalyst are shown in Fig. 13(e). Specifically, the addition of $CaTiO_3$ precipitated with Ni enhanced the rate of acetaldehyde decomposition, and the decomposition activity of acetaldehyde using $CaTiO_3$ precipitated with Ni was higher than that of ethanol.

CONCLUSIONS AND OUTLOOK

The generation of plasma in a liquid reactant aqueous solution results in the release of strong chemical oxidizing species as well as the emission of ultraviolet rays. During the LPP process, these strong oxidizing species and ultraviolet rays can be used to decompose water pollutants and produce hydrogen. Further, it was observed that hydrogen atom radicals as well as numerous electrons are generated in the plasma field formed owing to the LPP process. Taking advantage of these observations, metal nanoparticles can be synthesized by reducing metal ions, and metal nanoparticles can also be precipitated on various substrates.

Additionally, various water pollutants were successfully decomposed using the LPP process, and the effects of process variables, including plasma discharge conditions, dissolved oxygen concentration and pH on this water treatment method were examined. The effect of the addition of various photocatalysts, air bubbles and hydrogen peroxide on the reaction rate was also examined. Not only were several single-component metal nanoparticles synthesized using the LPP process, but bimetallic nanoparticles were also successfully synthesized. The effects of variables such as plasma discharge conditions, surfactant concentration, electrical conductivity, pH, precursor concentration and reaction time on the synthesis of nanoparticles were examined, and it was observed that the composition of two-component bimetallic nanoparticles can be adjusted by changing the concentration of the precursors. These previous studies also showed that various transition metals can be precipitated in carbon materials, including carbon nanotubes, graphene and activated carbon using the LPP process to prepare electrodes for secondary batteries and supercapacitors. Such electrodes precipitated with transition metals show large capacitance value and fast charging/discharging characteristics. Additionally, TiO_2 photocatalysts in which various kinds of metal nanoparticles were precipitated using the LPP process showed excellent visible light photoactivity. Using the LPP process only, it was possible to decompose water to produce hydrogen, and the addition of a photocatalyst resulted in a significant increase in the hydrogen production rate. When wastewater containing organic matter was treated using the LPP process, hydrogen could be produced with better efficiency, as the water pollutants were decomposed.

Recently, studies on the direct deposition of metals using various metal wires as electrodes via the LPP process and studies on the simultaneous preparation of nanocarbons and hydrogen by treating organic solvents using the LPP process have been attempted. These studies show that the LPP process can be easily and conveniently applied in one step. Therefore, its application in many fields is possible and its further development is expected.

We would like to insist on various possibilities in the future by introducing two examples of liquid phase plasma applied to actual sites. As a first example, the liquid plasma method can be used to recover fuel from gas hydrate layers that exist around Dokdo Island in Korea and in Japan's waters. In fact, Japan is pursuing this method and the concept is presented in Fig. 14 [58]. They are investigating a layer of methane hydrate with liquid phase plasma to recover hydrogen from gas hydrates in the deep ocean using a dehydrogenation reaction. So far, the use of a pump to recover methane hydrate has been considered. However, with the liquid phase plasma method, the required amount of hydrogen can be obtained from the gas hydrate layer on the sea floor without the need to use a pump.

The second, being carried out by a research team at Kumamoto University, is a device that removes the harmful microcystis aeruginosa (Fig. 15) [59]. As shown in the figure, it is a device equipped with a solar panel and a magnetic pulse compression type liquid phase plasma generator that kills microcystis aeruginosa by using the plasma generated by the floating type floating in the lake. The liquid phase plasma destroys the bubbles inside the microcystis aeru-

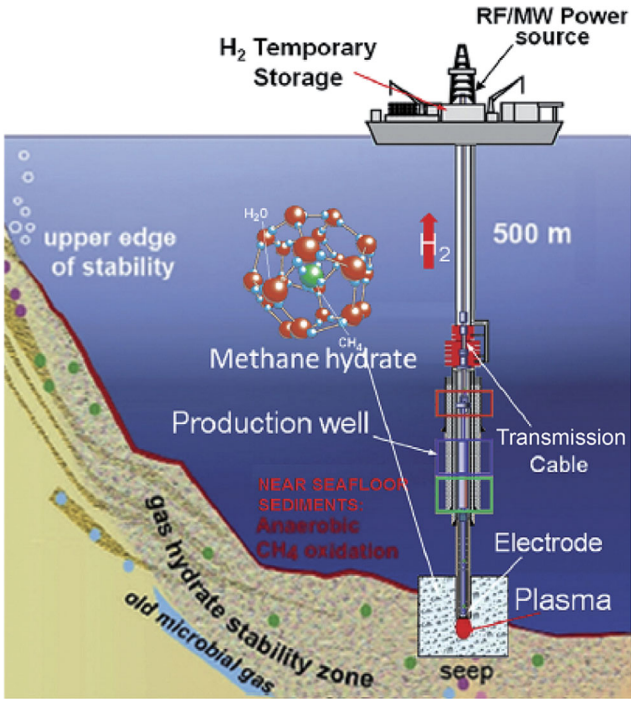

Fig. 14. Process for hydrogen production from hydrate fields in subsea sites using the plasma from the liquid phase plasma method. Reproduced from ref. [58]. Copyright 2015 by Elsevier.

Fig. 15. Photograph of a self-propelled liquid phase plasma apparatus floating over a dam to destroy the harmful Microcystis aeruginosa. Reproduced from ref. [59]. Copyright Kumamoto University, Japan.

ginosa cells, causing the microcystis aeruginosa to lose its buoyancy, and the blue patches thus treated sink into the lake and prevent further growth.

CONFLICT OF INTEREST

The authors have no conflict of interest.

REFERENCES

1. P. Baroch, V. Anita, N. Saito and O. Takai, *J. Electrostat.*, **66**, 294 (2008).
2. J. Hieda, N. Saito and O. Takai, *Surf. Coat. Tech.*, **202**, 5343 (2008).
3. N. Saito, J. H. Hieda and O. Takai, *Thin Solid Films*, **518**, 912 (2009).
4. P. Pootawang, N. Saito and O. Takai, *Thin Solid Films*, **519**, 7030 (2011).
5. M. Vijay, P. V. Ananthapadmanabhan and K. P. Sreekumar, *Appl. Surf. Sci.*, **255**, 9316 (2009).
6. J. S. Clements, M. Sato and R. H. Davis, *IEEE Trans. Ind. Appl.*, **IA-23**, 224 (1987).
7. K. Yasukoka, T. Haehara, J. Katsuki, S. Katsuki, T. Namihira, T. Kaneko and R. Hatakeyama, *J. Plasma Fusion Res.*, **84**, 666 (2008).
8. K. Schoenbach, J. Kolb, S. Xiao, S. Katsuki, Y. Minamitani and R. Joshi, *Plasma Sources Sci. Technol.*, **17**, 024010 (2008).
9. T. Namihira, S. Sakai, T. Yamaguchi, K. Yamamoto, C. Yamada, T. Kiyan, T. Sakugawa and S. Katsuki, *IEEE Trans. Plasma Sci.*, **35**, 614 (2007).
10. T. Tsuji, T. Mizuki, S. Ozono and M. Tsuji, *J. Photochem. Photobiol.*, A, **206**, 134 (2009).
11. R. Itatani, *Appl. Phys. Express*, **69**, 971 (2000).
12. M. Laroussi, *IEEE Trans. Plasma Sci.*, **24**, 1188 (1996).
13. J. S. Clements, M. Sato and R. H. Davis, *IEEE Trans. Ind. Appl.*, **IA-23**, 224 (1987).
14. J. C. Devins, S. J. Rzad and R. J. Schwabe, *J. Appl. Phys.*, **52**, 4531 (1981).
15. K. Yasukoka, T. Haehara, J. Katsuki, S. Katsuki, T. Namihira, T. Kaneko and R. Hatakeyama, *J. Plasma Fusion Res.*, **84**, 666 (2008).
16. A. Hickling and M. D. Ingram, *Trans. Faraday Soc.*, **60**, 783 (1964).
17. S. Horikoshi and N. Serpone, *RSC Adv.*, **7**, 47196 (2017).
18. T. Tsuji, T. Mizuki, S. Ozono and M. Tsuji, *J. Photochem. Photobiol.*, A, **206**, 134 (2009).
19. I. B. Gornushkin and U. Panne, *Spectrochim. Acta, Part B*, **65**, 345 (2000).
20. G. Saito and T. Akiyama, *J. Nanomater.*, **2015**, 1 (2015).
21. G. Sathyanarayanan, M. Haapala, C. Dixon, A. R. Wheeler and T. M. Sikanen, *Adv. Mater. Technol.*, 5: 2000451 (2020).
22. N. Mariotti, M. Bonomo, L. Fagiolari, N. Barbero, C. Gerbaldi, F. Bella and C. Barolo, *Green Chem.*, **22**, 7168 (2020).
23. A. Dokouzis, F. Bella, K. Theodosiou, C. Gerbaldi and G. Leftheriotis, *Mater. Today Energy*, **15**, 100365 (2020).
24. Z. Yang, Y. Luo, X. Gao and R. Wang, *Chem. Electro. Chem.*, **7**, 2599 (2020).
25. S. Galliano, F. Bella, M. Bonomo, G. Viscardi, C. Gerbaldi, G. Boschloo and C. Barolo, *Nanomaterials*, **10**, 1585 (2020).
26. M. Falco, C. Simari, C. Ferrara, J. R. Nair, G. Meligrana, F. Bella, I. Nicotera, P. Mustarelli, M. Winter and C. Gerbaldi, *Langmuir*, **35**, 8210 (2019).
27. B. R. Locke, M. Sato, P. Sunka, M. R. Hoffmann and J.-S. Chang, *Ind. Eng. Chem. Res.*, **45**, 882 (2006).
28. J. Noack and A. Vogel, *IEEE J. Quantum Electron.*, **35**, 1156 (1999).
29. S. Mukasa, S. Nomura and H. Toyota, *Jpn. J. Appl. Phys.*, **46**, 6015 (2007).
30. T. Maehara, H. Toyota, M. Kuramoto, A. Iwamae, A. Tadokoro, S. Mukasa, H. Yamashita, A. Kawashima and S. Nomura, *Jpn. J.*

Appl. Phys., **45**, 8864 (2006).
31. S. H. Sun and S.-C. Jung, *Korean J. Chem. Eng.*, **33**, 1075 (2016).
32. S. C. Kim, Y. K. Park, B. H. Kim, K. H. An, H. Lee, S. J. Lee and S. C. Jung, *J. Nanosci. Nanotechnol.*, **17**, 2578 (2017).
33. H. Lee, S. H. Park, S. J. Kim, Y. K. Park, B. J. Kim, K. H. An, S. J. Ki and S.-C. Jung, *Int. J. Hydrogen Energy*, **40**, 754 (2015).
34. S. J. Ki, Y.-K. Park, J.-S. Kim, W.-J. Lee, H. Lee and S.-C. Jung, *Chem. Eng. J.*, **377**, 120087 (2019).
35. S.-C. Kim, Y.-K. Park, B. H. Kim, H. Kim, W.-J. Lee, H. Lee and S.-C. Jung, *Korean J. Chem. Eng.*, **35**, 750 (2018).
36. S. J. Ki, K.-J. Jeon, Y.-K. Park, H. Park, S. Jeong, H. Lee and S.-C. Jung, *J. Environ. Manag.*, **203**, 880 (2017).
37. H. Lee, I.-S. Park, H.-J. Bang, Y.-K. Park, E.-B. Cho, B.-J. Kim and S.-C. Jung, *Appl. Surf. Sci.*, **481**, 625 (2019).
38. K.-H. Chung, H. Park, K.-J. Jeon, Y.-K. Park and S.-C. Jung, *Catal. Today*, **307**, 131 (2018).
39. K.-H. Chung, S. Jeong, H. Lee, S.-J. Kim, K.-J. Jeon, Y.-K. Park and S.-C. Jung, *Int. J. Hydrogen Energy*, **42**, 24099 (2017).
40. H. Lee, Y.-K. Park, J.-S. Kim, Y.-H. Park and S.-C. Jung, *Environ. Res.*, **169**, 256 (2019).
41. H. Lee, Y.-K. Park, S.-J. Kim, B.-H. Kim and S.-C. Jung, *Surf. Coat. Tech.*, **307**, 1018 (2016).
42. H. Lee, S. H. Park, C.-J. Cheong, S.-J. Kim, S.-G. Seo, Y.-K. Park and S.-C. Jung, *Ozone-Sci. Eng.*, **36**, 244 (2014).
43. Š. Potocký, N. Saito and O. Takai, *Thin Solid Films*, **518**, 918 (2009).
44. J. K. Lung, J. C. Huang, D. C. Tien, C. Y. Liao, K. H. Tseng, T. T. Tsung, W. S. Kao, T. H. Tsai, C. S. Jwo, H. M. Lin and L. Stobinski, *J. Alloys Compd.*, **434**, 655 (2007).
45. S. C. Kim, Y. K. Park, B. H. Kim, K. H. An, H. Lee, S. J. Lee and S. C. Jung, *J. Nanosci. Nanotechnol.*, **17**, 2578 (2017).
46. S.-J. Lee, H. Lee, K.-J. Jeon, H. Park, Y.-K. Park and S.-C. Jung, *Nanoscale Res. Lett.*, **11**, 344 (2016).
47. Z. Xu, C. Shen, Y. Tian, X. Shi and H. J. Gao, *Nanoscale*, **2**, 1027 (2010).
48. G. Bharath, R. madhu, S. M. Chen, V. Veeramani, D. Mangalaraja and N. Ponpandian, *J. Mater. Chem.* A, **3**, 15529 (2015).
49. F. Nensebaa, N. Patrito, Y. L. Page, P. L'Ecuyer and D. Wang, *J. Mater. Chem.*, **14**, 3378 (2014).
50. L. Ma, C. Liu, J. Liao, T. Lua, W. Xing and J. Zhang, *Electrochim. Acta*, **54**, 57274 (2009).
51. H. Lee, Y.-K. Park, S.-J. Kim, B.-H. Kim and S.-C. Jung, *Surf. Coat. Tech.*, **307**, 1018 (2016).
52. S. J. Ki, K.-J. Jeon, Y.-K. Park, H. Park, S. Jeong, H. Lee and S.-C. Jung, *J. Environ. Manage.*, **203**, 880 (2017).
53. B.-H. Kim, Y.-K. Park, K.-H. An, H. Lee and S.-C. Jung, *Sci. Adv. Mater.*, **8**, 1769 (2016).
54. K.-H. Chung, I.-S. Park, H.-J. Bang, Y.-K. Park, S.-J. Kim, B.-J. Kim and S.-C. Jung, *Sci. Total Environ.*, **676**, 190 (2019).
55. K.-H. Chung, S. Jeong, B.-J. Kim, J.-S. Kim, Y.-K. Park and S.-C. Jung, *Int. J. Hydrogen Energy*, **43**, 5873 (2018).
56. S. Jeong, K.-H. Chung, H. Lee, H. Park, K.-J. Jeon, Y.-K. Park and S.-C. Jung, *ACS Sustainable Chem. Eng.*, **5**, 3659 (2017).
57. K.-H. Chung, B.-J. Kim, S.-J. Kim, Y.-K. Park and S.-C. Jung, *Int. J. Hydrogen Energy*, **45**, 8595 (2018).
58. I. Rahim, S. Nomura, S. Mukasa and H. Toyota, *Appl. Therm. Eng.*, **90**, 120 (2015).
59. T. Sakugawa, N. Aoki, H. Akiyama, K. Ishibashi, M. Watanabe, A. Kouda and K. Suematsu, *IEEE Trans. Plasma Sci.*, **42**, 794 (2014).

Sang-chul Jung is currently a full professor at Sunchon National University, Department of Environmental Engineering. He received a B.S. and M.S. in Chemical Engineering from Chonnam National University and a Ph.D. in Engineering from Kyushu University. From 1995 to 1997 he worked at LG Semicon. His research interests include development of energy/environmental materials, liquid phase plasma process, surface and interface treatment.